

Modelling Fracture Mechanics Failure in Shales with Chemical Sensitivity

*Nnamdi E. Ezendiokwere*¹, *Ogbonna F. Joel*², *Victor J. Aimikhe*², and *Adewale Dosunmu*²

¹ *World Bank Africa Centre of Excellence, Centre for Oilfield Chemicals Research*

² *Department of Petroleum and Gas Engineering, University of Port Harcourt, Nigeria*

Received January 15, 2021; Accepted April 16, 2021

Abstract

One of the problems of shale formation is its chemical sensitivity, which characterizes shale capacity to undergo volume changes on exposure to water. The majority of the existing failure criteria models did not consider shale's chemical sensitivity at the micro-mechanical level. In this study, a new failure criterion similar to the Hoek-Brown failure criterion was developed for shales, using a combined micro-mechanical and fracture mechanics approach. This was carried out by incorporating the effect of chemical sensitivity in shales. Also, the effects of shale material properties like fracture coefficient, coefficient of friction, osmotic pressure, porosity, and pore fluid pressure on compressive failure stress were equally investigated. Using published laboratory data for Longmaxi shales, a comparative analysis of the failure stresses prediction of the Hoek-Brown, Mohr-Coulomb, and the failure criteria developed in this study was performed. The results obtained showed that the developed model followed the same trend as Hoek-Brown and Mohr-Coulomb failure criteria. It was also observed that the developed model had a closer agreement with the two failure criteria at low confining stresses. But at higher confining stress, the popular Hoek-Brown and Mohr-Coulomb failure criteria tend to overpredict shale rock strength. For instance, at 60 MPa, Hoek-Brown and Mohr-Coulomb failure criteria overpredicted the shale rock strength by 35.20% and 27.83%, respectively. While at higher confining stress of 100 MPa, Hoek-Brown and Mohr-Coulomb failure criteria overpredicted shale rock strength by 37.96% and 33.64%, respectively. The results of this study were equally found to be consistent with Griffith's theory of brittle failure.

Keywords: *Failure criterion; Shale; Wellbore instability; Micro-mechanics; Fracture mechanics; Chemical sensitivity.*

1. Introduction

Shale is phyllosilicate sedimentary rock derived from fine grains, clays, or silts, typically thinly laminated and weak. Shale is the most abundant sedimentary rock, and it is estimated to make up about 55% of all sedimentary rocks [6]. Figure 1 shows the classification of silicates into three groups: tectosilicates (framework silicates), phyllosilicates (sheet silicates), and others. Like other phyllosilicates, shale contains silicate sheets stacked one above the other. This structural arrangement makes it possible for small ions and water molecules to lodge between the silicate sheets, thereby causing swelling [2]. The properties of shale are highly influenced by depositional environment and post-depositional changes, especially diagenesis and compaction.

For instance, different colors in shales define the depositional environment of the sediments and their mineral composition. Colors in shale can be grouped into two major categories: gray-black and red-brown-yellow-green. Gray-black shales contain 1% or more free carbonaceous material, representing an oxygen-deficient environment. Red-brown-yellow-green colored shales show the presence or absence of iron oxide, including ferric oxide (red), hydroxide (brown), or limonite (yellow). In the absence of these mineral compounds, shale minerals' true green color (kaolinite, chlorite, and biotite) is dominant [6].

In addition, shales are also characterized by small porosities, with typical porosity values of less than 5% [3]. The small porosity values can be traced to the presence of fine grains, silt, and relatively high clay content, giving rise to small and largely unconnected pore spaces [17].

The small connected pores in the shale create permeability, which is very low compared to other sedimentary rocks. As a result, shales are usually known as permeability barriers to fluid and particle movement in general. Underlying low-permeability shale prevents downward movement of the water. On the other hand, the overlying shale caps seal hydrocarbons and prevent upward movement, thereby creating large pools of oil and gas reserves.

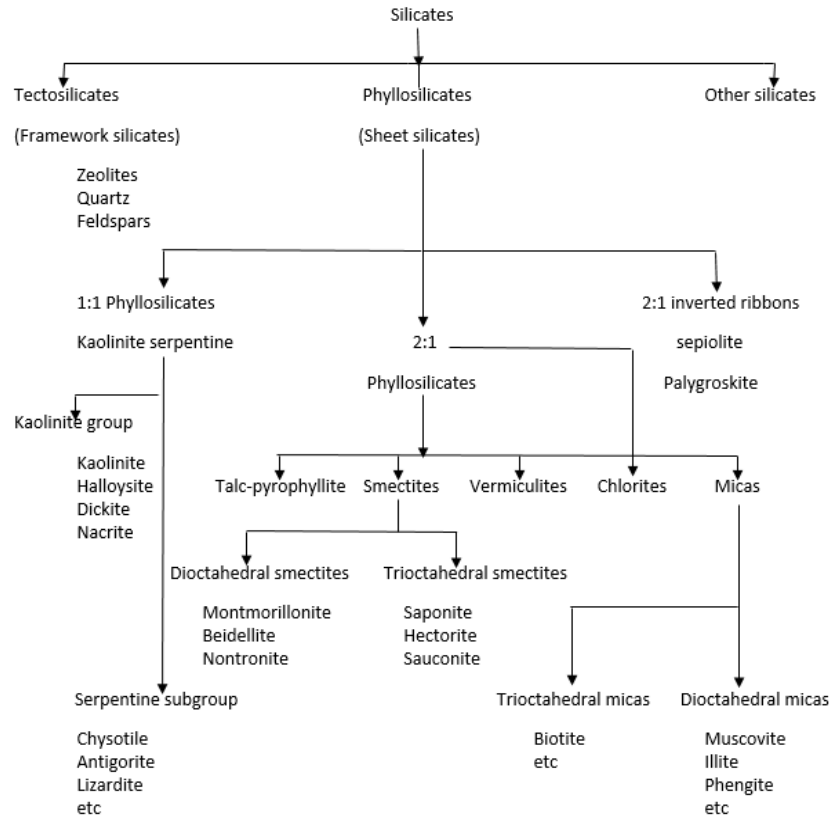


Figure 1. Classification of silicates [6]

Given that shale is the commonest sedimentary rock and petroleum is found in sedimentary basins, shale is frequently encountered in the petroleum industry. It has been reported that about 75% of all drilled formations are shales [4]. However, shale does not have a good reputation in the petroleum industry, as wellbore instability issues are attributed to its presence [18]. Consequences of wellbore instability include wellbore breakouts, washouts, damage of drilling equipment, gas kicks, or even ultimate loss of a drilled well. The consequences of wellbore instability related to shale contribute about 90% of the non-productive time during drilling, thereby costing the industry up to \$1 billion annually [4].

Moreover, wellbore instability occurs when a drilled formation is subjected to induced stress due to drilling beyond innate rock strength [7]. In chemically sensitive formations like shale, the induced stresses responsible for wellbore stability can be divided into geo-mechanical, chemical, and thermal. Geo-mechanical stresses arise as a result of the effect weight of overburden formations. Thermal stresses occur when there is a substantial temperature difference between the drilling mud and the formation. Chemical stress develops as a result of contact between phyllosilicate rocks like shales and water. By implication, geo-mechanical stress becomes more significant with increasing depth of burial, and chemical stress is found at shallow depths where there is less compaction.

In determining how rocks fail, rock failure criteria are frequently used. A rock failure criterion is simply a mathematical expression that uses rock material properties to predict the maximum stress a rock sample can withstand before it finally fails [13]. Available rock failure criteria can be divided into two-dimensional (2D) and three-dimensional (3D) rock failure

criteria [5]. Two-dimensional failure criteria do not consider the effect of the intermediate principal stress on rock failure, e.g., Mohr-Coulomb, Hoek-Brown, etc. Figure 2 shows the yield envelopes projected in the π -plane for various failure criteria. However, numerous experimental pieces of evidence abound, suggesting a substantial influence of the intermediate principal stress on rock failure. Hence, the three-dimensional failure criteria were developed to capture the effect of the intermediate principal stress, e.g., modified Lade, modified Wiebols-Cook, Drucker-Preger, etc. [24].

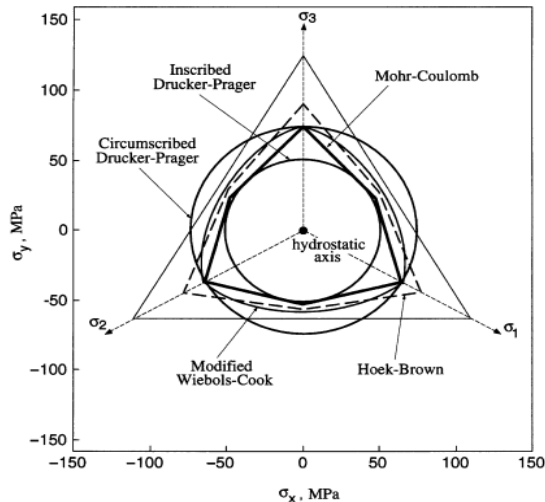


Figure 2. Yield envelopes projected in the π -plane for the Mohr-Coulomb criterion, the Hoek and Brown criterion, the modified Wiebols and Cook criterion, and the circumscribed and inscribed Drucker-Prager criterion [24]

Meanwhile, most rock failure models currently in use were derived empirically [26]. This means that they were developed by fitting a generalized mathematical expression to a large volume of experimental rock failure data. Rock failure criteria have also been developed using micro-mechanical analysis and fracture mechanics. The building block of the micro-mechanical treatment of rock failure is Griffith's theory of brittle failure. According to Griffith's theory, the low level of strength in brittle materials can be attributed to the presence of microcracks or flaws. This failure theory is especially true for brittle materials like glass but is equally applicable to rocks whose state of stress is not beyond the brittle-ductile transition point [28].

Consequently, numerous researchers have successfully used micro-mechanical analysis and fracture mechanics to develop failure criteria. Perhaps, notable among them

is the recent theoretical derivation of the Hoek-Brown failure criterion for rock materials by Zuo *et al.* [28]. Also, Zuo *et al.* [25] derived a gas-mechanical coupled constitutive equation for fractured coal containing gas. It is the opinion of the authors that such micro-mechanical and fracture mechanics treatment could be extended to shale. This is because, using the convenience of modern equipment like scanning electron microscope (SEM) and X-ray computed tomography, the existence of Griffith cracks has been confirmed in several materials, including argillaceous rocks like shale. Also, shale is typically laminated [17], and in the presence of discontinuities of varying orientations, cracks of arbitrary orientation can easily be found. The presence of lamination increases its likelihood of failure through propagation and coalescence of critical miniature cracks and fractures, thereby rendering it amenable to coupled micro-mechanical and fracture mechanics treatment. In addition, conventional rock failure criteria incorporate chemical sensitivity by adding it as additional stress to the principal stress components. Still, there seems to be no analytical model that has incorporated chemical sensitivity in shale at the micro-mechanical level.

In this study, a coupled micro-mechanical and fracture mechanics failure criterion for shale is presented based on a sliding Griffith crack model, which considers chemical sensitivity in shale. This was done to investigate the influence of chemical reactivity (typical of shale formations) and other shale properties on shale's compressive failure.

2. Model development

The Cauchy stress representation gives an actual state of stress for any material under different stress configurations [4]. But the six stress components can be resolved into the three principal stresses [24]. Hence, for simplification, only the three principal stresses are considered here. According to Griffith's theory, intact solids are replete with microcracks responsible for their failure. In applying this theory, the following additional assumptions are made [25]:

- (a) The shale sample under consideration contains countless discontinuities such that there exist numerous randomly distributed Griffith cracks.
- (b) Microcracks are very much isolated from each other that they do not interact.
- (c) The shale matrix containing the microcracks is believed to exhibit material isotropy
- (d) The embedded cracks are not open under the existing stress field.

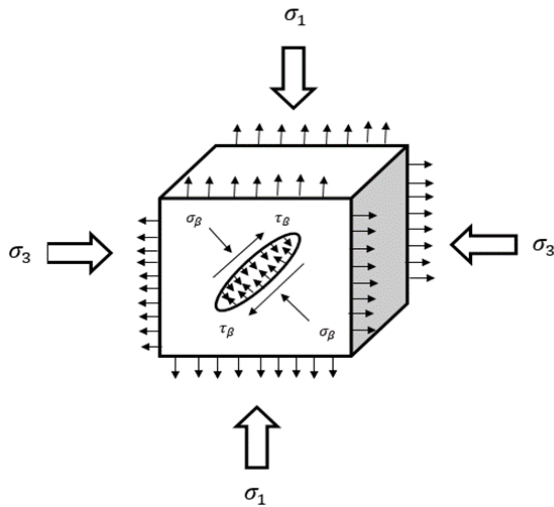


Figure 3. A representative volume element of a shale sample under volumetric osmotic pressure showing infiltrating fluid within a sliding crack

The numerous discontinuities found in rocks usually lead to a local concentration of stress that can cause the growth of pre-existing microcracks. In representing these microcracks, elliptical sliding cracks of crack length, $2a$ at a given angle β to the maximum principal stress, are frequently used. For porous-fluid materials like shale, these microcracks are filled with infiltrating fluids, as shown in Figure 3. Also, the strength of shales is known to be dependent on their chemical sensitivity when in contact with water [7]. This usually results in a heaving or shrinkage process depending on relative water activities of shale and the invading drilling mud. In effect, this gradually reduces strength in shales as exposure to water continues [18]. The heaving mechanism involves a volumetric expansion that acts in opposi-

tion to compressional geological stress, as shown in Figure 3. The shrinkage involves a volumetric reduction in size as fluids diffuse outwards under osmotic pressure. For this study, only the external principal stresses, normal stress, shear stress, pore pressure and osmotic pressures are considered.

The normal and shear stresses are given by [24]:

$$\sigma_\beta = \frac{1}{2}(\sigma_1 + \sigma_3) + \frac{1}{2}(\sigma_1 - \sigma_3) \cos 2\beta \quad (1)$$

$$\tau_\beta = \frac{1}{2}(\sigma_1 - \sigma_3) \sin 2\beta \quad (2)$$

where σ_β and τ_β are normal, and shear stresses, respectively.

By incorporating pore and hydration pressures, we have:

$$\sigma_n = \frac{1}{2}(\sigma_1 + \sigma_3) + \frac{1}{2}(\sigma_1 - \sigma_3) \cos 2\beta - \theta p - P_\pi \quad (3)$$

$$\tau_n = \frac{1}{2}(\sigma_1 - \sigma_3) \sin 2\beta \quad (4)$$

where: θ is shale porosity; p is pore fluid pressure; P_π is osmotic pressure; σ_n is net normal stress; τ_n is net shear stress.

From above, it can be seen that the net shear stress is equal to the initial shear stress ($\tau_n = \tau_\beta$), this can be attributed to the fact that both fluid and osmotic pressures have fluid origins. Hence, they are volumetric and are not expected to support shear stress. Typically, the net shear stress arising from the principal stresses controls deformation by promoting crack sliding, which leads to failure. However, the net normal stress would always stop the sliding motion by providing frictional stress counteracting the motion. Consequently, the effective shear stress is given by:

$$\tau_e = \tau_n - \mu \sigma_n \quad (5)$$

$$= \frac{1}{2}(\sigma_1 - \sigma_3) \sin 2\beta - \mu \left[\frac{1}{2}(\sigma_1 + \sigma_3) + \frac{1}{2}(\sigma_1 - \sigma_3) \cos 2\beta - \theta p - P_\pi \right] \quad (6)$$

where μ is the coefficient of friction.

If the effective shear stress is high enough to propagate the initial crack, this can lead to a local concentration of tensile stress at the tip of the initial pre-existing crack. If this tensile stress continues for some time, it leads to nucleation of adjoining wing cracks, as shown in

Figure 4a. Before crack propagation begins for a sliding mode of deformation, the initial crack tip's stress intensity factor is given by [14]:

$$K_{II} = \tau_e(\pi a)^{1/2} \quad (7)$$

Following linear elastic fracture mechanics principles, for infinitesimal crack length, the stress intensity factor at the tip of the secondary crack is [16]:

$$K_{II} \geq kK_{IC} \quad (8)$$

where k is the constant of kinked cracks, which depends on the type of failure criterion. For maximum stress criteria, $k = \sqrt{3}/2$ [21], for minimum strain energy criteria, $k = \sqrt{3(1-v)/(2+2v-v^2)}$ (where v is Poisson's ratio), according to [19], and $k = 1$ for maximum energy release rate criteria [28]. Then, the fracture toughness K_{IC} can be expressed using induced tensile strength σ_t and crack length a by [25]:

$$K_{IC} = \sigma_t(\pi a)^{1/2} \quad (9)$$

Substituting Eq. (7) and (9) into (8), the effective shear stress can be expressed as:

$$\tau_e \geq k\sigma_t \quad (10)$$

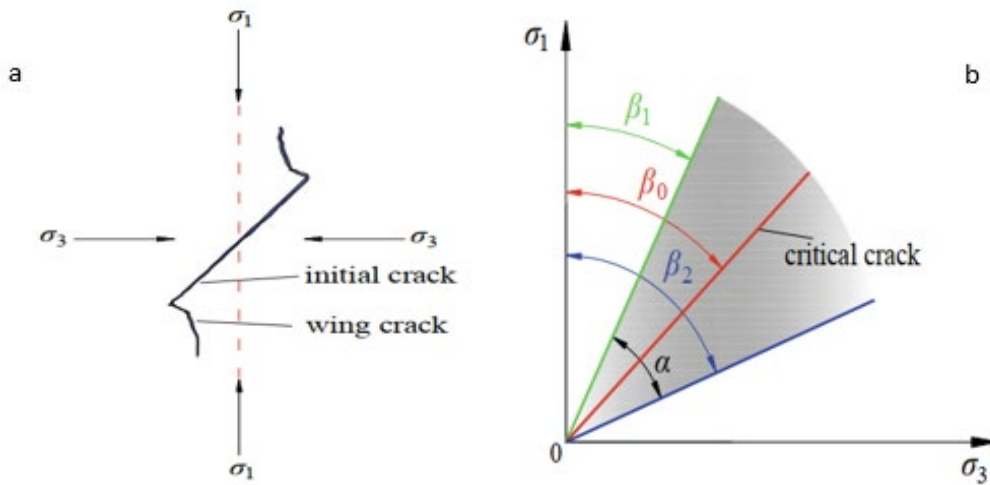


Figure 4. (a) Propagation of wing cracks from the tip of an initial crack (b) Crack distribution zone [26]

2.1. Micro-failure orientation angle (α)

Allowing the lower ends and points of all wingcracks that satisfy Eq 10 to converge., a fan-shaped area of crack distribution will emerge in the $\sigma_1 - \sigma_3$ plane. The resulting included angle α , in the $\sigma_1 - \sigma_3$ plane is known as the micro-failure orientation angle. This angle defines the orientation of all fitting wingcracks, as shown in Figure 4b.

Mathematically,

$$\alpha = \beta_2 - \beta_1 \quad (11)$$

Substituting Eq. (6) into (10), we have:

$$\frac{1}{2}(\sigma_1 - \sigma_3) \sin 2\beta - \mu \left[\frac{1}{2}(\sigma_1 + \sigma_3) + \frac{1}{2}(\sigma_1 - \sigma_3) \cos 2\beta - \theta p - P_\pi \right] \geq k\sigma_t \quad (12)$$

Recall from trigonometric identities of double angles,

$$\sin 2\beta = \frac{2 \tan \beta}{1 + \tan^2 \beta} \quad (13)$$

$$\cos 2\beta = \frac{1 - \tan^2 \beta}{1 + \tan^2 \beta} \quad (14)$$

Substituting Eqs. (13) and (14) into (12):

$$\frac{1}{2}(\sigma_1 - \sigma_3) \cdot \left(\frac{2 \tan \beta}{1 + \tan^2 \beta} \right) - \mu \left[\frac{1}{2}(\sigma_1 + \sigma_3) + \frac{1}{2}(\sigma_1 - \sigma_3) \cdot \left(\frac{1 - \tan^2 \beta}{1 + \tan^2 \beta} \right) - \theta p - P_\pi \right] \geq k\sigma_t \quad (15)$$

Multiplying both sides by $2(1 + \tan^2 \beta)$, we have:

$$2(\sigma_1 - \sigma_3) \tan \beta - \mu \sigma_1 (1 + \tan^2 \beta) - \mu \sigma_3 (1 + \tan^2 \beta) - \mu (\sigma_1 - \sigma_3) (1 - \tan^2 \beta) + 2\mu \theta p (1 + \tan^2 \beta) + 2\mu P_\pi (1 + \tan^2 \beta) - 2(1 + \tan^2 \beta) k\sigma_t \geq 0 \quad (16)$$

Simplifying and collecting like terms,

$$+\mu\sigma_1 \tan^2 \beta - \mu\sigma_1 \tan^2 \beta - \mu\sigma_3 \tan^2 \beta - \mu\sigma_3 \tan^2 \beta + 2\mu\theta p \tan^2 \beta + 2\mu P_\pi \tan^2 \beta - 2k\sigma_t \tan^2 \beta + 2\sigma_1 \tan \beta - 2\sigma_3 \tan \beta - \mu\sigma_1 - \mu\sigma_1 + \mu\sigma_3 - \mu\sigma_3 + 2\mu\theta p + 2\mu P_\pi - 2k\sigma_t \geq 0 \quad (17)$$

On further simplification and factorization,

$$(2\mu\theta p - 2\mu\sigma_3 + 2\mu P_\pi - 2k\sigma_t) \tan^2 \beta + 2(\sigma_1 - \sigma_3) \tan \beta - 2\mu\sigma_1 + 2\mu\theta p + 2\mu P_\pi - 2k\sigma_t \geq 0 \quad (18)$$

Dividing both sides by $-2\sigma_t$,

$$\left(\mu\hat{\sigma}_3 - \frac{\mu\theta p}{\sigma_t} - \frac{\mu P_\pi}{\sigma_t} + k\right) \tan^2 \beta - (\hat{\sigma}_1 - \hat{\sigma}_3) \tan \beta + \mu\hat{\sigma}_1 - \frac{\mu\theta p}{\sigma_t} - \frac{\mu P_\pi}{\sigma_t} + k \leq 0 \quad (19)$$

Where

$$\hat{\sigma}_1 = \frac{\sigma_1}{\sigma_t} \quad (20)$$

$$\hat{\sigma}_3 = \frac{\sigma_3}{\sigma_t} \quad (21)$$

The solution of the above quadratic equation gives $\tan \beta$ such that,

$$\tan \beta_1 \leq \tan \beta \leq \tan \beta_2 \quad (22)$$

Recall that the standard expression for a quadratic equation is:

$$ax^2 + bx + c = 0 \quad (23)$$

and its solution is given by:

$$x = \frac{-b \pm \sqrt{b^2 - 4ac}}{2a} \quad (24)$$

Comparing Eq. (19) above with Eq. (23),

$$a = \left(\mu\hat{\sigma}_3 - \frac{\mu\theta p}{\sigma_t} - \frac{\mu P_\pi}{\sigma_t} + k\right), \quad b = -(\hat{\sigma}_1 - \hat{\sigma}_3), \quad c = \left(\mu\hat{\sigma}_1 - \frac{\mu\theta p}{\sigma_t} - \frac{\mu P_\pi}{\sigma_t} + k\right) \quad (25)$$

Substituting accordingly,

$$\tan \beta_1 = \frac{(\hat{\sigma}_1 - \hat{\sigma}_3) - \sqrt{(\hat{\sigma}_1 - \hat{\sigma}_3)^2 - 4\left(\mu\hat{\sigma}_3 - \frac{\mu\theta p}{\sigma_t} - \frac{\mu P_\pi}{\sigma_t} + k\right)\left(\mu\hat{\sigma}_1 - \frac{\mu\theta p}{\sigma_t} - \frac{\mu P_\pi}{\sigma_t} + k\right)}}{2\left(\mu\hat{\sigma}_3 - \frac{\mu\theta p}{\sigma_t} - \frac{\mu P_\pi}{\sigma_t} + k\right)} \quad (26)$$

$$\tan \beta_2 = \frac{(\hat{\sigma}_1 - \hat{\sigma}_3) + \sqrt{(\hat{\sigma}_1 - \hat{\sigma}_3)^2 - 4\left(\mu\hat{\sigma}_3 - \frac{\mu\theta p}{\sigma_t} - \frac{\mu P_\pi}{\sigma_t} + k\right)\left(\mu\hat{\sigma}_1 - \frac{\mu\theta p}{\sigma_t} - \frac{\mu P_\pi}{\sigma_t} + k\right)}}{2\left(\mu\hat{\sigma}_3 - \frac{\mu\theta p}{\sigma_t} - \frac{\mu P_\pi}{\sigma_t} + k\right)} \quad (27)$$

Meanwhile, let

$$A = (\hat{\sigma}_1 - \hat{\sigma}_3) \quad (28)$$

$$B = 2\left(\mu\hat{\sigma}_3 - \frac{\mu\theta p}{\sigma_t} - \frac{\mu P_\pi}{\sigma_t} + k\right) \quad (29)$$

$$C = (\hat{\sigma}_1 - \hat{\sigma}_3)^2 - 4\left(\mu\hat{\sigma}_3 - \frac{\mu\theta p}{\sigma_t} - \frac{\mu P_\pi}{\sigma_t} + k\right)\left(\mu\hat{\sigma}_1 - \frac{\mu\theta p}{\sigma_t} - \frac{\mu P_\pi}{\sigma_t} + k\right) \quad (30)$$

So that Eqs. (26) and (27) can be written as:

$$\tan \beta_1 = \frac{A - \sqrt{C}}{B} \quad (31)$$

$$\tan \beta_2 = \frac{A + \sqrt{C}}{B} \quad (32)$$

But from Eq. (11), the micro-failure orientation is given as:

$$\alpha = (\beta_2 - \beta_1) \text{ So, } \tan \alpha = \tan(\beta_2 - \beta_1) \quad (33)$$

Also, from trigonometric identities,

$$\tan(\beta_2 - \beta_1) = \frac{\tan \beta_2 - \tan \beta_1}{1 + \tan \beta_2 \tan \beta_1} \quad (34)$$

For the numerator,

$$\tan \beta_2 - \tan \beta_1 = \frac{(A + \sqrt{C})}{B} - \frac{(A - \sqrt{C})}{B} = \frac{2\sqrt{C}}{B} \quad (35)$$

And for the denominator,

$$1 + \tan \beta_2 \tan \beta_1 = 1 + \frac{(A + \sqrt{C})}{B} \times \frac{(A - \sqrt{C})}{B} = \frac{A^2 - C + B^2}{B^2} \quad (36)$$

Hence, combining Eqs. (35) and (36),

$$\frac{\tan \beta_2 - \tan \beta_1}{1 + \tan \beta_2 \tan \beta_1} = \frac{2\sqrt{C}}{B} \times \frac{B^2}{A^2 - C + B^2} = \frac{2B\sqrt{C}}{A^2 - C + B^2} \quad (37)$$

Then, substituting accordingly,

$$\tan \alpha = \frac{2 \left[2 \left(\mu \hat{\sigma}_3 - \frac{\mu \theta p}{\sigma_t} - \frac{\mu P_\pi}{\sigma_t} + k \right) \cdot \sqrt{(\hat{\sigma}_1 - \hat{\sigma}_3)^2 - 4 \left(\mu \hat{\sigma}_3 - \frac{\mu \theta p}{\sigma_t} - \frac{\mu P_\pi}{\sigma_t} + k \right) \cdot \left(\mu \hat{\sigma}_1 - \frac{\mu \theta p}{\sigma_t} - \frac{\mu P_\pi}{\sigma_t} + k \right)}{(\hat{\sigma}_1 - \hat{\sigma}_3)^2 - (\hat{\sigma}_1 - \hat{\sigma}_3)^2 - 4 \left(\mu \hat{\sigma}_3 - \frac{\mu \theta p}{\sigma_t} - \frac{\mu P_\pi}{\sigma_t} + k \right) \cdot \left(\mu \hat{\sigma}_1 - \frac{\mu \theta p}{\sigma_t} - \frac{\mu P_\pi}{\sigma_t} + k \right) + \left[2 \left(\mu \hat{\sigma}_3 - \frac{\mu \theta p}{\sigma_t} - \frac{\mu P_\pi}{\sigma_t} + k \right) \right]^2} \quad (38)$$

On simplification,

$$\tan \alpha = \frac{\sqrt{(\hat{\sigma}_1 - \hat{\sigma}_3)^2 - 4 \left(\mu \hat{\sigma}_3 - \frac{\mu \theta p}{\sigma_t} - \frac{\mu P_\pi}{\sigma_t} + k \right) \cdot \left(\mu \hat{\sigma}_1 - \frac{\mu \theta p}{\sigma_t} - \frac{\mu P_\pi}{\sigma_t} + k \right)}}{\mu(\hat{\sigma}_1 + \hat{\sigma}_3) + 2 \left[k - \frac{\mu}{\sigma_t}(\theta p + P_\pi) \right]} \quad (39)$$

But Eq. (39) can also be expressed as:

$$\tan \alpha = \frac{\sqrt{(\hat{\sigma}_1 - \hat{\sigma}_3)^2 - 4 \left(\mu \hat{\sigma}_3 - \frac{\mu \theta p}{\sigma_t} - \frac{\mu P_\pi}{\sigma_t} + k \right) \cdot \left(\mu \hat{\sigma}_1 - \frac{\mu \theta p}{\sigma_t} - \frac{\mu P_\pi}{\sigma_t} + k \right)}}{\mu(\hat{\sigma}_1 + \hat{\sigma}_3) + 2 \left[k - \frac{\mu}{\sigma_t}(\theta p + P_\pi) \right]} \times \frac{(\hat{\sigma}_1 - \hat{\sigma}_3) \cdot (\sqrt{1 + \mu^2})}{(\hat{\sigma}_1 - \hat{\sigma}_3) \cdot (\sqrt{1 + \mu^2})} \quad (40)$$

Or rearranged as:

$$\tan \alpha = \frac{\sqrt{(\hat{\sigma}_1 - \hat{\sigma}_3)^2 - 4 \left(\mu \hat{\sigma}_3 - \frac{\mu \theta p}{\sigma_t} - \frac{\mu P_\pi}{\sigma_t} + k \right) \cdot \left(\mu \hat{\sigma}_1 - \frac{\mu \theta p}{\sigma_t} - \frac{\mu P_\pi}{\sigma_t} + k \right)}}{(\hat{\sigma}_1 - \hat{\sigma}_3) \cdot (\sqrt{1 + \mu^2})} \times \frac{(\hat{\sigma}_1 - \hat{\sigma}_3) \cdot (\sqrt{1 + \mu^2})}{\mu(\hat{\sigma}_1 + \hat{\sigma}_3) + 2 \left[k - \frac{\mu}{\sigma_t}(\theta p + P_\pi) \right]} \quad (41)$$

$$\text{Meanwhile, from basic trigonometry, } \tan \alpha = \frac{\sin \alpha}{\cos \alpha} \quad (42)$$

So that comparing Eqs. (41) and (42),

$$\cos \alpha = \frac{\mu(\hat{\sigma}_1 + \hat{\sigma}_3) + 2 \left[k - \frac{\mu}{\sigma_t}(\theta p + P_\pi) \right]}{(\hat{\sigma}_1 - \hat{\sigma}_3) \cdot (\sqrt{1 + \mu^2})} \quad (43)$$

2.2. Rock failure characteristic parameter

According to [26], a rock failure characteristic parameter can be expressed as: $\frac{\partial \cos \alpha}{\partial \hat{\sigma}_1}$

Therefore, differentiating Eq. (43) with respect to $\hat{\sigma}_1$,

$$\frac{\partial \cos \alpha}{\partial \hat{\sigma}_1} = \frac{-2\mu \left\{ \hat{\sigma}_3 + \frac{k}{\mu} - \frac{1}{\sigma_t}(\theta p + P_\pi) \right\}}{(\hat{\sigma}_1 - \hat{\sigma}_3)^2 \cdot (\sqrt{1 + \mu^2})} \quad (44)$$

For uniaxial compression tests, $\hat{\sigma}_1 = \hat{\sigma}_c$ and $\hat{\sigma}_3 = 0$, hence, Eq. (44) becomes,

$$\frac{\partial \cos \alpha}{\partial \hat{\sigma}_1} = \frac{-2\mu \left[\frac{k}{\mu} - \frac{1}{\sigma_t}(\theta p + P_\pi) \right]}{(\hat{\sigma}_c)^2 \cdot (\sqrt{1 + \mu^2})} \quad (45)$$

Equating Eqs. (44) and (45), while rearranging to make $\hat{\sigma}_1$ the subject, we have:

$$\hat{\sigma}_1 = \hat{\sigma}_3 + \hat{\sigma}_c \left(\frac{\mu \hat{\sigma}_3}{\left[k - \frac{\mu}{\sigma_t}(\theta p + P_\pi) \right]} + 1 \right)^{1/2} \quad (46)$$

Changing $\hat{\sigma}_1, \hat{\sigma}_3, \hat{\sigma}_c$ back to $\sigma_1/\sigma_t, \sigma_3/\sigma_t, \sigma_c/\sigma_t$ respectively and multiplying both sides by σ_t ,

$$\sigma_1 = \sigma_3 + \sigma_c \left(\frac{\mu}{\left[k\sigma_t - \mu(\theta p + P_\pi) \right]} \sigma_3 + 1 \right)^{1/2} \quad (47)$$

and comparing Eq. (47) with Hoek-Brown rock failure criterion for intact rocks as expressed below,

$$\sigma_1 = \sigma_3 + \sigma_{ci} \left(\frac{m_i}{\sigma_{ci}} \sigma_3 + 1 \right)^{1/2} \quad (48)$$

It is obvious that,

$$\frac{m_i}{\sigma_{ci}} = \frac{\mu}{\left[k\sigma_t - \mu(\theta p + P_\pi) \right]} \quad (49)$$

So,

$$m_i = \frac{\mu \sigma_{ci}}{\left[k\sigma_t - \mu(\theta p + P_\pi) \right]} \quad (50)$$

3. Numerical analysis

Table 1 shows the range of shale properties values from different sources used for this study's numerical analysis. Cohesion, tensile strength, and porosity values were obtained from experimental studies carried out on Longmaxi shale from Sichuan basin in China. Fracture coefficient values were obtained from the possible values of k as stated, while also considering the possible Poisson ratio of shale to lie between 0.1-0.5. Friction coefficient values used were within the typical range of friction coefficient values for most rocks. The osmotic pressure values included both hydrating and dehydrating values, including values for a wide range of shale samples like Arco-China and Pierre shales. It is known that negative osmotic pressures lead to hydration of shale and subsequent volumetric expansion, while positive osmotic pressures lead to dehydration of shale and subsequent volumetric shrinkage [7]. Therefore, in this study, the response of shale on exposure to water is divided into negative and positive osmotic pressure effects.

Also, the fluid pore pressures were assumed based on values encountered in field operations. The pore pressure is not expected to be higher than the shale tensile strength, except during hydraulic fracturing. Hence, the tensile strength provided a bound for the pore fluid pressure assumptions. Table 2 shows the base values equally used for the numerical analysis obtained by taking the average of the property ranges in Table 1. To ensure a proper basis for effective analysis and comparison, the failure stress results discussed were for uniaxial compression. This decision was taken due to this type of test's popularity, which allows for a simpler and yet enriching discussion of the results to be carried out. The influence of the minimum principal stress (confining stress) on the results obtained were also investigated and are given in Tables 3-8 in the Appendix. While Table 9 compares predictions of failure stress from the developed model with Hoek-Brown and Mohr-Coulomb failure criteria.

Table 1. Shale parameter values used for numerical analysis.

Parameter (unit)	Symbol	Value	Source
Cohesion (MPa)	S_o	22.50-29.64	[17]
Tensile strength (MPa)	σ_t	0.43-8.22	[17]
Porosity (%)	θ	2.05-5.80	[3]
Fracture coefficient (-)	k	0.50-2.00	[26]
Friction coefficient (-)	μ	0.20-0.80	[26]
Osmotic pressure-hydrating (MPa)	P_π	-0.02-(-0.30)	[18]
Osmotic pressure-dehydrating (MPa)	P_π	0.057-0.48	[18]
Pore fluid pressure (MPa)	p	0.00-8.00	Assumed

Table 2. Shale parameter base values used for numerical analysis

Parameter (unit)	Symbol	Base values
Cohesion (MPa)	S_o	25.61
Tensile strength (MPa)	σ_t	4.33
Porosity (%)	θ	3.93
Fracture coefficient (-)	k	1.25
Friction coefficient (-)	μ	0.50
Osmotic pressure-hydrating (MPa)	P_π	-0.16
Osmotic pressure-dehydrating (MPa)	P_π	0.27
Pore fluid pressure (MPa)	p	4.00

Figures 5-10 were generated by varying fracture coefficient, coefficient of friction, osmotic pressure, porosity, and pore fluid pressure respectively at zero confining stress while keeping the other variables constant at their average values as depicted in Table 2. In Figure 11, Longmaxi shale laboratory data from [23] was utilized. Tensile and shear stress data in the form of the conventional Mohr-Coulomb failure curve were first converted to its corresponding linearized form similar to Eq. (52). This was carried out by obtaining the linearized Mohr-Coulomb parameter by exploiting the relationship between the coefficient of friction and angle of internal friction, as given in Eqs. (53) and (54). The obtained linearized Mohr-Coulomb

parameter was later used in generating the Mohr-Coulomb failure curve. Confining and failure stress values from the linearized Mohr-Coulomb failure curve was also used to obtain the corresponding Hoek-Brown parameter. This was achieved by plotting $(\sigma_1 - \sigma_3)^2$ against σ_3 and then obtaining the Hoek-Brown parameter from the slope of the resulting straight line. The obtained Hoek-Brown parameter was then used in generating the Hoek-Brown failure curve. While the average shale properties in Table 2 were used in generating the failure curve for the developed model.

The uniaxial compressive strength [24] is given as:

$$\sigma_c = 2S_o[(\mu^2 + 1)^{\frac{1}{2}} + \mu] \tag{51}$$

and the linearized Mohr-Coulomb failure criterion that was equally used is given by [5]:

$$\sigma_1 = \sigma_c + q\sigma_3 \tag{52}$$

$$q = [(\mu^2 + 1)^{\frac{1}{2}} + \mu]^2 = \tan^2\left(\frac{\pi}{4} + \phi/2\right) \tag{53}$$

$$\phi = \tan^{-1}(\mu) \tag{54}$$

where q is linearized Mohr-Coulomb parameter and ϕ is the angle of internal friction.

4. Results and discussion

Figure 5 shows the variation of uniaxial compression failure stress with fracture coefficient at different pore pressures, depicting an inverse proportionality relation between failure stress and fracture coefficient. This relationship indicates that shale failure stress will reduce with an increase in fracture coefficient. The fracture coefficient is also directly proportional to the stress intensity factor at the tip of existing cracks [14]. As a result, the higher the fracture coefficient, the higher the stress intensity at existing crack tips, which makes failure occur with the application of increasingly lower stress. Figure 5 also shows that the fracture coefficient's influence on compressive failure stress gradually decreases as the fracture coefficient increases.

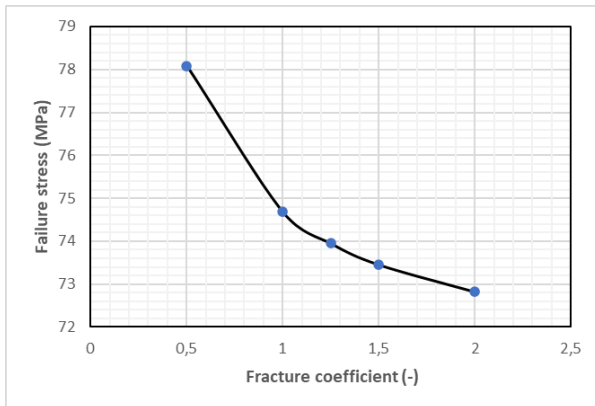


Figure 5. Variation of uniaxial compression failure stress with fracture coefficient

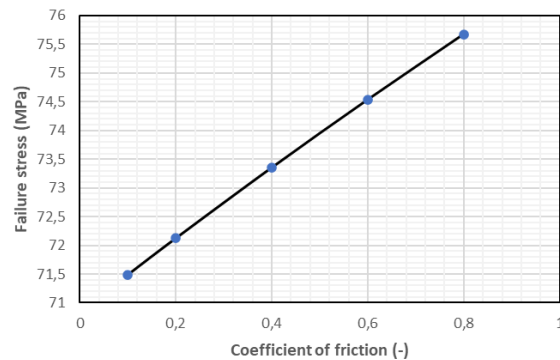


Figure 6. Variation of uniaxial compression failure stress with coefficient of friction

Figure 6 shows the variation of uniaxial compression failure stress with the coefficient of friction at different pore pressures. It shows that there is a direct proportionality between failure stress and friction coefficient. Implying that as the coefficient of friction of a shale sample increases, so will the corresponding compressive failure. This is because the higher the coefficient of friction, the more difficult it becomes for a shale sample to fail by sliding mode because of increased friction. This, in turn, increases the amount of compressive stress needed to ultimately cause failure in a given shale sample [28].

Figure 7 shows the variation of uniaxial compression failure stress with negative osmotic pressures at different pore pressures. An inverse relationship between compressive failure stress and negative shale osmotic pressure can be noticed from the figure. This means that at increasing negative osmotic pressure, a given shale sample's compressive failure stress will monotonically reduce. Negative osmotic pressure is generated when shale water activity is higher than drilling mud water activity [18]. This condition leads to hydration of shale and ultimately volumetric expansion (or heaving), thereby increasing the likelihood of failure.

Since increasing negative osmotic pressure increases the likelihood of failure, an increasingly less amount of compressive stress will be required for the shale sample to fail.

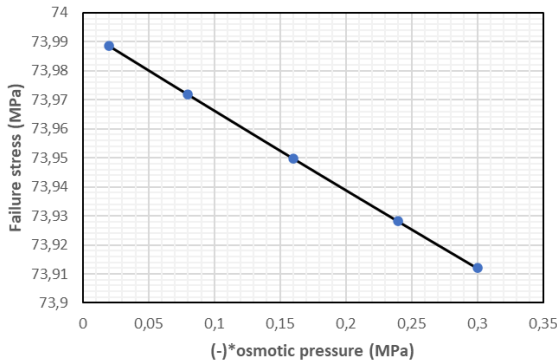


Figure 7. Variation of uniaxial compression failure stress with negative osmotic pressures

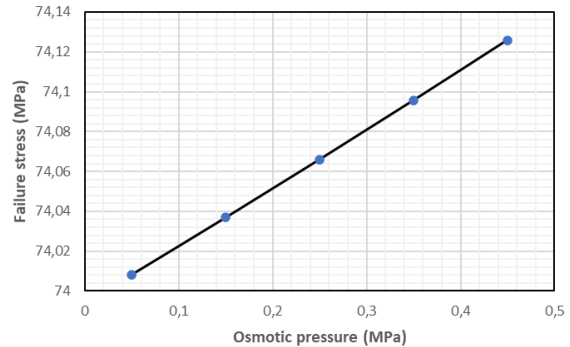


Figure 8. Variation of uniaxial compression failure stress with positive osmotic pressures

On the other hand, Figure 8 shows the variation of uniaxial compression failure stress with positive osmotic pressures at different pore pressures. It can be deduced that there exists a direct proportionality between compressive failure stress and positive osmotic pressure. This implies that compressive failure stress will generally reduce on increasing positive osmotic pressure. Positive osmotic pressure is generated in shales when shale water activity is lower than drilling mud water activity [18]. And this condition causes dehydration in shale, as water will diffuse out of any given shale sample under positive osmotic pressure [7]. This process results in further compaction due to the shale's net volumetric shrinkage, thereby reducing the likelihood of shale compressive failure, which in turn increases the compressive failure stress.

Figure 9 shows the variation of uniaxial compression failure stress with porosity at different pore pressures. From the figure, an inverse proportionality is noticed between compressive failure stress and porosity. What this implies is that increasingly lower compressive failure stress will be needed as porosity increases in shale. The brittle failure of porous solid materials is known to be strongly influenced by their inherent porosity called micro-cracks [26]. Such that porous materials with higher porosities tend to fail quicker than materials of low porosity under compressive stress [13]. Since shale is a porous rock material, the behavior depicted by Figure 9 is believed to follow similar failure mechanism. Hence, the higher the number of these micro-cavities in shale (equivalent to higher porosity), the easier compressive rock failure occurs. This, in turn, leads to lower compressive stress requirements before failure ultimately happens. On the other hand, the lower the micro-cavities (equivalent to low porosity), the higher the compressive stress needed to cause failure in shale.

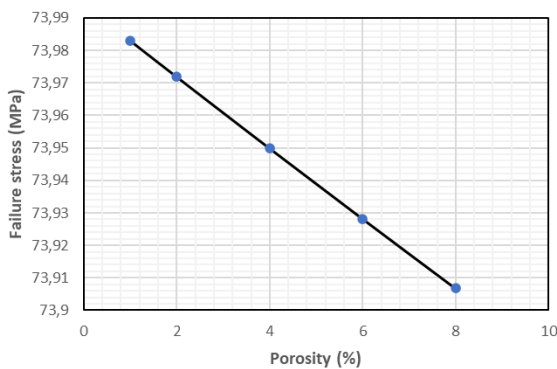


Figure 9. Variation of uniaxial compression failure stress with porosity

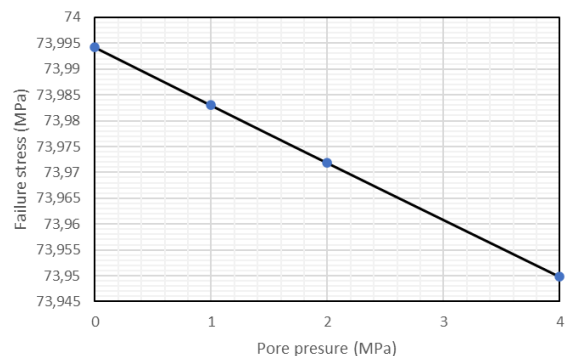


Figure 10. Variation of uniaxial compression failure stress with pore pressure

Figure 10 shows the variation of uniaxial compression failure stress with pore pressure. From the figure, an inverse proportionality between compressive failure stress and pore

pressure is observed. This means that compressive failure stress increases as pore pressures in cracks and voids present in shale increase. This behavior is in agreement with general rock mechanics principles given the way pore pressures are exerted. Pore pressures are generally known to counteract compressive stress. Hence, pore pressures act in such a way that it tends to reduce compressive stress giving rise to the concept of effective stress [25]. Therefore, it will take higher compressive stress for a shale sample to break at lower pore pressures compared to lower compressive stress at higher pore pressures.

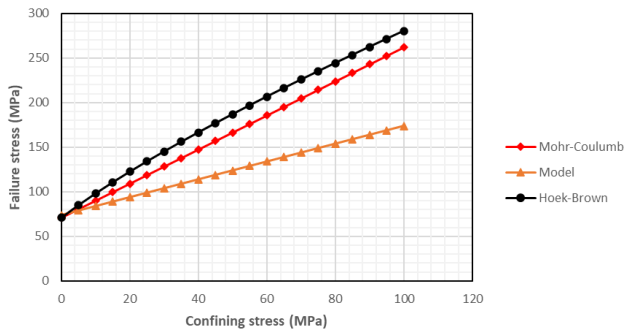


Figure 11. Comparison of the developed model with Hoek-Brown and Mohr-Coulomb failure criteria

Figure 11 shows a comparison of the developed model with Hoek-Brown and Mohr-Coulomb failure criteria. The figure shows that the model followed a linear trend like the popular failure criteria. The figure equally reveals a closer agreement between the developed model and the other failure criteria at low confining stress. This trend can be explained by the fact that the influence of shale chemical sensitivity on rock strength increases with confining stress [1]. As a result, at low confining stress, the effect of

chemical sensitivity on rock strength can be considered insignificant. But as the confining stress was increasing, the difference between the failure stress predicted by the developed model and the other failure criteria was also increasing.

This increasing difference can be attributed to the fact the popular Hoek-Brown and Mohr-Coulomb failure criteria are empirical models [26] and, as such, did not consider the influence of chemical sensitivity in shale. Moreover, chemical sensitivity in shale negatively affects rock strength [18], such that with increasing confining stress, a given shale sample will fail more easily compared to failure in the absence of chemical stress [1]. This explains why the model developed in this study gave lower compressive failure stresses at corresponding confining stresses.

In addition, it can also be seen from Figure 11 that the developed model followed the same straight-line trend as Hoek-Brown and Mohr-Coulomb failure criteria. It is also evident that the popular Hoek-Brown and Mohr-Coulomb failure criteria tend to overpredict shale rock strength at higher confining stress. For instance, at 60 MPa, Hoek-Brown and Mohr-Coulomb failure criteria overpredicted shale rock strength by 35.20% and 27.83%, respectively. At higher confining stress of 100 MPa, Hoek-Brown and Mohr-Coulomb failure criteria overpredicted shale rock strength by 37.96% and 33.64%, respectively. Therefore, care should be taken when using the Hoek-Brown and Mohr-Coulomb failure criteria, especially at depths where the shale chemical sensitivity is significant.

5. Conclusion

A new shale compressive failure model incorporating chemical sensitivity for shales have been developed. The relationship between compressive failure stress and shale properties like friction coefficient, osmotic pressure, porosity, and pore pressure was also presented.

The Hoek-Brown and Mohr-Coulomb failure criteria were found to overpredict shale rock strength at high confining stresses than this study's developed failure model, by 35.20% and 27.83%, respectively, at confining stress of 60 MPa, and by 37.96% and 33.64%, respectively, at confining stress of 100MPa.

Symbols

θ	shale porosity (%)	S_o	Cohesion (MPa)
p	pore fluid pressure (MPa)	σ_t	Tensile strength (MPa)
P_π	osmotic pressure (MPa)	k	Fracture coefficient (-)
σ_n	net normal stress (MPa)	μ	Friction coefficient (-)
τ_n	net shear stress (MPa)		

Appendix

Table 3. Sensitivity of failure stress at varying confining stress to fracture coefficient

σ_3 (MPa)	σ_1 (MPa)				
	k=0.5	k= 1	k=1.25	k= 1.5	k=2
5	83.08656	79.68023	78.94985	78.45297	77.82026
10	88.08656	84.68023	83.94985	83.45297	82.82026
15	93.08656	89.68023	88.94985	88.45297	87.82026
20	98.08656	94.68023	93.94985	93.45297	92.82026
25	103.0866	99.68023	98.94985	98.45297	97.82026
30	108.0866	104.6802	103.9498	103.453	102.8203
35	113.0866	109.6802	108.9498	108.453	107.8203
40	118.0866	114.6802	113.9498	113.453	112.8203
45	123.0866	119.6802	118.9498	118.453	117.8203
50	128.0866	124.6802	123.9498	123.453	122.8203
55	133.0866	129.6802	128.9498	128.453	127.8203
60	138.0866	134.6802	133.9498	133.453	132.8203
65	143.0866	139.6802	138.9498	138.453	137.8203
70	148.0866	144.6802	143.9498	143.453	142.8203
75	153.0866	149.6802	148.9498	148.453	147.8203
80	158.0866	154.6802	153.9498	153.453	152.8203
85	163.0866	159.6802	158.9498	158.453	157.8203
90	168.0866	164.6802	163.9498	163.453	162.8203
95	173.0866	169.6802	168.9498	168.453	167.8203
100	178.0866	174.6802	173.9498	173.453	172.8203

Table 4. Sensitivity of failure stress at varying confining stress to coefficient of friction

σ_3 (MPa)	σ_1 (MPa)				
	$\mu=0.1$	$\mu = 0.2$	$\mu =0.4$	$\mu = 0.6$	$\mu =0.8$
5	76.4876	77.12193	78.35261	79.53556	80.67393
10	81.4876	82.12193	83.35261	84.53556	85.67393
15	86.4876	87.12193	88.35261	89.53556	90.67393
20	91.4876	92.12193	93.35261	94.53556	95.67393
25	96.4876	97.12193	98.35261	99.53556	100.6739
30	101.4876	102.1219	103.3526	104.5356	105.6739
35	106.4876	107.1219	108.3526	109.5356	110.6739
40	111.4876	112.1219	113.3526	114.5356	115.6739
45	116.4876	117.1219	118.3526	119.5356	120.6739
50	121.4876	122.1219	123.3526	124.5356	125.6739
55	126.4876	127.1219	128.3526	129.5356	130.6739
60	131.4876	132.1219	133.3526	134.5356	135.6739
65	136.4876	137.1219	138.3526	139.5356	140.6739
70	141.4876	142.1219	143.3526	144.5356	145.6739
75	146.4876	147.1219	148.3526	149.5356	150.6739
80	151.4876	152.1219	153.3526	154.5356	155.6739
85	156.4876	157.1219	158.3526	159.5356	160.6739
90	161.4876	162.1219	163.3526	164.5356	165.6739
95	166.4876	167.1219	168.3526	169.5356	170.6739
100	171.4876	172.1219	173.3526	174.5356	175.6739

Table 5. Sensitivity of failure stress at varying confining stress to negative osmotic pressures

σ_3 (MPa)	σ_1 (MPa)				
	$P_\pi = -0.02$	$P_\pi = -0.08$	$P_\pi = -0.16$	$P_\pi = -0.24$	$P_\pi = -0.30$
5	78.98857	78.97185	78.94985	78.92815	78.91207
10	83.98857	83.97185	83.94985	83.92815	83.91207
15	88.98857	88.97185	88.94985	88.92815	88.91207
20	93.98857	93.97185	93.94985	93.92815	93.91207
25	98.98857	98.97185	98.94985	98.92815	98.91207
30	103.9886	103.9719	103.9498	103.9281	103.9121
35	108.9886	108.9719	108.9498	108.9281	108.9121
40	113.9886	113.9719	113.9498	113.9281	113.9121
45	118.9886	118.9719	118.9498	118.9281	118.9121
50	123.9886	123.9719	123.9498	123.9281	123.9121
55	128.9886	128.9719	128.9498	128.9281	128.9121
60	133.9886	133.9719	133.9498	133.9281	133.9121
65	138.9886	138.9719	138.9498	138.9281	138.9121
70	143.9886	143.9719	143.9498	143.9281	143.9121
75	148.9886	148.9719	148.9498	148.9281	148.9121
80	153.9886	153.9719	153.9498	153.9281	153.9121
85	158.9886	158.9719	158.9498	158.9281	158.9121
90	163.9886	163.9719	163.9498	163.9281	163.9121
95	168.9886	168.9719	168.9498	168.9281	168.9121
100	173.9886	173.9719	173.9498	173.9281	173.9121

Table 6. Sensitivity of failure stress at varying confining stress to positive osmotic pressures

σ_3 (MPa)	σ_1 (MPa)				
	$P_\pi = 0.05$	$P_\pi = 0.15$	$P_\pi = 0.25$	$P_\pi = 0.35$	$P_\pi = 0.45$
5	79.00829	79.0369	79.06603	79.0957	79.12592
10	84.00829	84.0369	84.06603	84.0957	84.12592
15	89.00829	89.0369	89.06603	89.0957	89.12592
20	94.00829	94.0369	94.06603	94.0957	94.12592
25	99.00829	99.0369	99.06603	99.0957	99.12592
30	104.0083	104.0369	104.066	104.0957	104.1259
35	109.0083	109.0369	109.066	109.0957	109.1259
40	114.0083	114.0369	114.066	114.0957	114.1259
45	119.0083	119.0369	119.066	119.0957	119.1259
50	124.0083	124.0369	124.066	124.0957	124.1259
55	129.0083	129.0369	129.066	129.0957	129.1259
60	134.0083	134.0369	134.066	134.0957	134.1259
65	139.0083	139.0369	139.066	139.0957	139.1259
70	144.0083	144.0369	144.066	144.0957	144.1259
75	149.0083	149.0369	149.066	149.0957	149.1259
80	154.0083	154.0369	154.066	154.0957	154.1259
85	159.0083	159.0369	159.066	159.0957	159.1259
90	164.0083	164.0369	164.066	164.0957	164.1259
95	169.0083	169.0369	169.066	169.0957	169.1259
100	174.0083	174.0369	174.066	174.0957	174.1259

Table 7. Sensitivity of failure stress at varying confining stress to shale porosity

σ_3 (MPa)	σ_1 (MPa)				
	$\theta = 1$	$\theta = 2$	$\theta = 4$	$\theta = 6$	$\theta = 8$
5	78.98298	78.97185	78.94985	78.92815	78.90675
10	83.98298	83.97185	83.94985	83.92815	83.90675
15	88.98298	88.97185	88.94985	88.92815	88.90675
20	93.98298	93.97185	93.94985	93.92815	93.90675
25	98.98298	98.97185	98.94985	98.92815	98.90675
30	103.983	103.9719	103.9498	103.9281	103.9067
35	108.983	108.9719	108.9498	108.9281	108.9067
40	113.983	113.9719	113.9498	113.9281	113.9067
45	118.983	118.9719	118.9498	118.9281	118.9067
50	123.983	123.9719	123.9498	123.9281	123.9067
55	128.983	128.9719	128.9498	128.9281	128.9067
60	133.983	133.9719	133.9498	133.9281	133.9067
65	138.983	138.9719	138.9498	138.9281	138.9067
70	143.983	143.9719	143.9498	143.9281	143.9067
75	148.983	148.9719	148.9498	148.9281	148.9067
80	153.983	153.9719	153.9498	153.9281	153.9067
85	158.983	158.9719	158.9498	158.9281	158.9067
90	163.983	163.9719	163.9498	163.9281	163.9067
95	168.983	168.9719	168.9498	168.9281	168.9067
100	173.983	173.9719	173.9498	173.9281	173.9067

Table 8. Sensitivity of failure stress at varying confining stress to pore pressure

σ_3 (MPa)	σ_1 (MPa)			
	$p = 0$	$p = 1$	$p = 2$	$p = 4$
5	78.99418	78.98298	78.97185	78.94985
10	83.99418	83.98298	83.97185	83.94985
15	88.99418	88.98298	88.97185	88.94985
20	93.99418	93.98298	93.97185	93.94985
25	98.99418	98.98298	98.97185	98.94985
30	103.9942	103.983	103.9719	103.9498
35	108.9942	108.983	108.9719	108.9498
40	113.9942	113.983	113.9719	113.9498
45	118.9942	118.983	118.9719	118.9498
50	123.9942	123.983	123.9719	123.9498
55	128.9942	128.983	128.9719	128.9498
60	133.9942	133.983	133.9719	133.9498
65	138.9942	138.983	138.9719	138.9498
70	143.9942	143.983	143.9719	143.9498
75	148.9942	148.983	148.9719	148.9498
80	153.9942	153.983	153.9719	153.9498
85	158.9942	158.983	158.9719	158.9498
90	163.9942	163.983	163.9719	163.9498
95	168.9942	168.983	168.9719	168.9498
100	173.9942	173.983	173.9719	173.9498

Table 9. Comparison of the developed model with Hoek-Brown and Mohr-Coulomb failure criteria

σ_3 (MPa)	σ_1 (MPa)		
	Mohr-Coulomb	Hoek-Brown	Model
0	70.83947	70.83947	73.95061
5	80.40352	84.96203	78.95061
10	89.96756	98.14546	83.95061
15	99.5316	110.6312	88.95061
20	109.0956	122.572	93.95061
25	118.6597	134.072	98.95061
30	128.2237	145.2059	103.9506
35	137.7878	156.0293	108.9506
40	147.3518	166.5851	113.9506
45	156.9159	176.9071	118.9506
50	166.4799	187.0226	123.9506
55	176.0439	196.9538	128.9506
60	185.608	206.7194	133.9506
65	195.172	216.335	138.9506
70	204.7361	225.8139	143.9506
75	214.3001	235.1676	148.9506
80	223.8642	244.4061	153.9506
85	233.4282	253.538	158.9506
90	242.9922	262.571	163.9506
95	252.5563	271.5119	168.9506
100	262.1203	280.3667	173.9506

Acknowledgement

The authors are grateful to the Petroleum Technology Development Fund (PTDF), Nigeria, for sponsoring this research with grant number PTDF-SP&D-AOGRG-V.III-117-011B. Grant is for the experiment, data gathering, processing, and report writing.

References

- [1] Al-Bazali TM. Experimental study of the membrane behavior of shale during interaction with water-based and oil-based muds, Doctoral dissertation, University of Texas at Austin. 2005.
- [2] Cantillo V, Mercado V, Pájaro C. Empirical correlations for the swelling pressure of expansive clays in the city of Barranquilla, Colombia. *Earth Sci. Res. J.* 2017; 21(1): 45-49.
- [3] Chen F, Lu S, Ding X, Zhao H, Ju Y. Total porosity measured for shale gas reservoir samples: A Case from the Lower Silurian Longmaxi formation in Southeast Chongqing, China. *Minerals.* 2019; 9(5): 1-12.
- [4] Cheng AH-D. *Poroelasticity*; Springer: Zurich, 2016.
- [5] Colmenares LB, Zoback MD. A statistical evaluation of intact rock failure criteria constrained by polyaxial test data for five different rocks. *International Journal of Rock Mechanics & Mining Sciences.* 2002; 39(2002): 695-729.
- [6] Farrokhrouz M, Asef MR. *Shale engineering: Mechanics and mechanisms*; Taylor & Francis: Florida, 2013.
- [7] Fernández-Vera WA, Corzo R, Saavedra NF. Selection of oil-based mud salinity through effective osmotic pressure evaluation in Carbonera shale for Colombian foothills. *Ciencia, Tecnología y Futuro.* 2010; 4(1): 23-37.
- [8] Griffith AA. The phenomena of rupture and flow in solids. *Philos Trans R Soc Lond (Ser A).* 1921; 221(2): 163-198.
- [9] Heidug WK, Wong S. Hydration swelling of water-absorbing rocks: A constitutive model. *International Journal for Numerical and Analytical Methods in Geomechanics.* 1996; 20: 403-430.
- [10] Hoek E, Brown E. Empirical strength criterion for rock masses. *J Geotech Eng Div,* 1980; 106(GT9): 1013-1035.
- [11] Hoek E, Brown E. The Hoek-Brown failure criterion: A 1988 update. Presented at the 15th Canadian Rock Mech. Symp (Edited by Curran J. C.), 1988.
- [12] Hoek E, Brown E. Practical estimates of rock mass strength. *Int J Rock Mech Min Sci.* 1997; 34(8): 1165-1186.

- [13] Hoek E, Brown E. The Hoek-Brown failure criterion and GSI-2018 edition. *J Rock Mech Geotech Eng.* 2018.
- [14] Jaeger JC, Cook NGW, Zimmerman RW. *Fundamentals of rock mechanics*; Blackwell: London, 2010.
- [15] Kachanov ML. A microcrack model of rock inelasticity, Part I: frictional sliding on microcracks. *Mech Mater.* 1982a; 1: 19–27.
- [16] Kachanov ML. A microcrack model of rock inelasticity, Part II: propagation of microcracks. *Mech Mater.* 1982b; 1: 29–41.
- [17] Li L, Huang B, Huang X, Wang M, Li X. Tensile and shear mechanical characteristics of Longmaxi shale laminae dependent on the mineral composition and morphology. *Energies.* 2020; 13: 2977–2985.
- [18] Luo X, Were P, Hou Z, Gou Y. Determination of shale osmotic pressure using spontaneous potential log. *Environ Earth Sci.* 2017; 76(19): 1–8.
- [19] Nuismer RJ. An energy release rate criterion for mixed mode fracture. *Int J Fract,* 1975; 11(2): 245– 250.
- [20] Sih GC. Strain-energy-density factor applied to mixed mode crack problems. *Int J Fract,* 1974; 10(3): 305–321.
- [21] Sih GC, Macdonald B. Fracture mechanics applied to engineering problems-strain-energy density fracture criterion. *Eng Frac Mech.* 1974; 6(2): 361–386.
- [22] Tada H. *Stress analysis of cracks handbook*; Del Research Corporation: Hellertown, 1973.
- [23] Wu Y., Li X., He J. and Zheng B. Mechanical properties of Longmaxi black organic-rich shale samples from South China under uniaxial and triaxial compression states, *Energies*, 2016; 9, 1088. doi:10.3390/en9121088.
- [24] Zoback MD. *Reservoir Geomechanics.* Cambridge University Press: United Kingdom, 2007.
- [25] Zuo J, Jiang G, Wei W, Su H. A gas-mechanical coupled constitutive equation for fractured coal containing gas. *J Nat Gas Sci & Eng.* 2016; 36: 1109–1119.
- [26] Zuo J, Shen J. *The Hoek-Brown Failure criterion-From theory to application*; Springer Nature: Singapore, 2020.
- [27] Zuo JP, Li HT, Xie HP, Ju Y, Peng SP. A nonlinear strength criterion for rocklike materials based on fracture mechanics. *Int J Rock Mech Min Sci.* 2008; 45(4): 594–9.
- [28] Zuo JP, Liu HH, Li HT. A theoretical derivation of the Hoek-Brown failure criterion for rock materials. *J Rock Mech Geotech Eng.* 2015; 7(4): 361–6.

To whom correspondence should be addressed: Dr. Nnamdi E. Ezendiokwere, World Bank Africa Centre of Excellence, Centre for Oilfield Chemicals Research, Nigeria, E-mail: nnamdi_ezendiokwere@uniport.edu.ng